

High-performing germanium-silicon single-photon avalanche diode operated at room temperature

Neil Na^{1*}, Yen-Cheng Lu¹, Yu-Hsuan Liu^{1,2}, Po-Wei Chen¹, Ying-Chen Lai¹, You-Ru Lin¹,
Chung-Chih Lin^{1,2}, Tim Shia¹, Chih-Hao Cheng¹, and Shu-Lu Chen¹

¹Artlux Inc., Zhubei City, Hsinchu County, Taiwan, ROC

²National Tsing-Hua University, Hsinchu City, Hsinchu County, Taiwan, ROC

*Email: neil@artiluxtech.com

The capability of detecting single photons has greatly advanced a wide range of research fields such as optical quantum information processing¹⁻⁶, bio-photonics⁷, and light detection and ranging (LiDAR)⁸⁻¹¹. While various types of single-photon detectors have been developed¹², due to two main factors, i.e., 1) the need of operating at cryogenic temperature, e.g., superconducting nanowire single-photon detectors (SNSPD)^{13,14}, and 2) the incompatibility with complementary metal-oxide-semiconductor (CMOS) fabrication process, e.g., III-V based single-photon avalanche diode (SPAD)^{15,16}, so far only Si-based SPAD^{17,18} has gained mainstream success and been used in consumer electronics such as smart phones and wearables. However, with growing demand in migrating the operation wavelength from near-infrared (NIR) to short-wavelength infrared (SWIR) for better safety and performance¹⁹⁻²¹, alternative solution is required since Si has negligible optical absorption for wavelengths beyond 1 μm . Ge-based SPAD, which is CMOS compatible and can detect SWIR, may be a suitable candidate and has been extensively studied in the literature²²⁻³¹, but generally showed high dark count rate (DCR) and/or low single-photon detection probability (SPDP) so that decent performance can only be reached at a low temperature typically < 200 K. Here we demonstrate a high-performing GeSi SPAD operated at room temperature, featuring a noise-equivalent power (NEP) improvement over the previously reported Ge-based SPADs by 2 to 3.5 orders of magnitude. Key parameters such as DCR, SPDP, timing jitter, after-pulsing probability (APP) and characteristic time are investigated in detail, and three-dimensional (3D) point-cloud (PCL) images are captured with direct time-of-flight (TOF) technique as proof of concept. This work paves the path toward ubiquitous deployment of single-photon sensitive, SWIR optoelectronic sensors and imagers as well as photonic integrated circuits in daily life applications.

Detectors that are extremely sensitive and may discern the smallest quanta of light, i.e., a single photon, are referred as single-photon detectors. These detectors have played crucial roles in the past decades in scientific researches on optical quantum computation^{1,2}, quantum key distribution^{3,4}, and quantum imaging^{5,6}, by detecting the granular properties of light, and in recent technological developments of LiDAR in coaxial setting with single detectors^{8,9}, or in camera setting with pixel arrays^{10,11}, by time-resolving the photon arrival events. Solid-state implementations of such detectors through superconductors and semiconductors are perhaps the most well-known choices. A classic example using superconductors would be SNSPD, which is biased just below its critical current

point and so when a photon is absorbed the resultant local resistive spot would trigger a voltage pulse to the external circuit. Another classic example using semiconductors would be SPAD, or sometimes referred as Geiger-mode avalanche photodiode (APD), which is biased slightly above its breakdown voltage point and so when a photon is absorbed the resultant impact ionization would trigger a current pulse to the external circuit. While SNSPD may detect a broad wavelength range from mid-infrared to visible, it typically operates at a cryogenic temperature of a few K¹²⁻¹⁴ that limits its usage mainly as a lab instrument. On the other hand, SPAD with InGaAs or Si may only detect specific wavelength range from SWIR to NIR or from NIR to visible, respectively, but they can be operated at room temperature or near room temperature^{12,15-18} and hence became popular for general purposes. For InGaAs-based SPAD, the device commonly consists of InGaAs layer for absorption and InP layer for multiplication, so that absorption and multiplication can be separately engineered for optimized performance^{15,16}. For Si-based SPAD, the device commonly consists of p+/n or n+/p junction where absorption and multiplication occur in the same region, so that design trade-offs such as quantum efficiency and breakdown voltage are often made^{17,18}. Nevertheless, Si-based SPAD is intrinsically CMOS compatible, and the integration with CMOS circuits at sub-micron technology node under front-side illumination¹⁷ or at deep sub-micron technology node under back-side illumination¹⁸ has been demonstrated. Such powerful advancements have made Si-based SPAD enter the segment of mainstream consumer electronics as proximity sensors and 3D imagers at NIR. Recently, SWIR has emerged as the next-generation choice of wavelength due to the following reasons: 1) better laser eye-safety since NIR can cause damage to retina¹⁹, 2) lower ambient light interference since solar spectrum is weaker at SWIR or even absent around 1380 nm wavelength²⁰, 3) higher atmospheric transmission since free-space optical transmissivity is dominated by Rayleigh scattering that is inversely proportional to wavelength²¹, and 4) less interference with Si devices and circuits as Si absorbs NIR but not SWIR. Consequently, SWIR single-photon detectors that can be operated at room temperature and are CMOS compatible are actively sought after. In the literature, Ge-based SPAD may be a potential candidate, and can be generally categorized into several groups such as low-Ge-content SiGe on Si as separate-absorption-charge-multiplication (SACM) heterojunction device²², Ge as p+/n or n+/p homojunction device²³, Ge on Si as SACM heterojunction device²⁴⁻²⁹, and low-Sn-content GeSn on Si as SACM heterojunction device³⁰. However, these works either experimentally showed high DCR and/or low SPDP so that decent performance can only be reached at a low temperature typically < 200 K, or included only simulation data without experimental supports.

In this paper, we report the fabrication of a 15 μm diameter GeSi SPAD with CMOS compatible fabrication process, and characterize it at room temperature to demonstrate its high performance. To benchmark the demonstrated GeSi SPAD and the Ge-based SPADs in the literature, we calculate the NEP by using the definition³¹

$$NEP = \frac{h\omega\sqrt{2 \cdot DCR}}{SPDP}, \quad (1)$$

where the DCR and SPDP from the highest operation voltages at the highest operation temperatures are used in the calculations. In Fig. 1, the NEP and the operation temperature of Ref. [22-28] and this work are plotted, and, except for Ref. [22] that operates at 300 K but features a NEP that is at least 3 orders of magnitude higher than that of the

demonstrated GeSi SPAD, all other Ge-based SPADs operate at a low temperature ranging from 77 K to 200 K and so their NEP cannot be fairly compared at a common temperature. To better estimate the difference in NEP, without loss of generality, the increase of DCR with temperature is assumed to double every 10 K³¹, which is typical for Ge-based devices with activation energy close to mid-bandgap. Then, the dashed-dotted arrows in Fig. 1 indicate the NEP of the previously reported Ge-based SPADs if they were operated at 300 K, so that clear comparisons can be made: the demonstrated GeSi SPAD features an unprecedentedly low NEP about a few fW/ $\sqrt{\text{Hz}}$ at room temperature, which is 2 to 3.5 orders of magnitude lower than those of the previously reported Ge-based SPADs. The drastic difference is mainly contributed to the low dark current of the demonstrated GeSi SPAD. Taking Ref. [24] as an example, which is the first demonstration of Ge-on-Si SACM APD for SPAD, it features a dark current about 1 μA at the punch-through point around -22 V, whereas the demonstrated GeSi SPAD features a dark current about 20 pA at the punch-through point around -9 V (to be shown in later paragraphs). Note that in Fig. 1 the device areas are not normalized, because for the previously reported Ge-based SPADs the DCR depends highly on design and process and does not scale well with the device area (e.g., Ref. [27] has an area about 15 times larger than that of Ref. [28] but their NEP are about the same). Still the demonstrated GeSi SPAD has a NEP that is on average 2.5 orders of magnitude lower than that of the previously reported Ge-based SPADs if the device areas are normalized.

The significant reduction of the dark current of the demonstrated GeSi SPAD is made possible by addressing the following issues: 1) the threading dislocations occurring on the (311) planes in Ge arisen from the 4% lattice-mismatch between Ge and Si, 2) the lack of high-quality surface passivation agents over Ge surfaces, and 3) the high electric fields at low-quality material regions. For the issue of threading dislocation, various methods have been pursued such as graded buffer layers grown between Si and Ge³², post-Ge high-temperature thermal annealing³³, low-energy plasma-enhanced chemical vapor deposition (CVD)³⁴, high-aspect-ratio trapping of defects³⁵, and Ge-on-insulator with defects chemically-mechanically polished³⁶, to name a few. For the issue of surface passivation, various agents have been experimented such as amorphous Si³⁷, GeO₂³⁸, Al₂O₃³⁶, and pure Ga/B³⁹, to name a few. Generally, with the combined efforts of reducing threading dislocations and surface dangling bonds, Ge-on-Si photodiode (PD) featuring a low dark current density between tens to hundreds of $\mu\text{A}/\text{cm}^2$ can be accomplished at a low reverse-bias voltage. However, to be used as a high-performing APD or even SPAD, such a low dark current must be maintained while the device is biased above the unity gain point, in which high reverse-bias voltages are applied to create the high electric fields needed for transporting photo-carriers and generating impact ionizations. In fact, the previously reported Ge-based APD, e.g., Ge-on-Si SACM APD⁴⁰⁻⁴² and Ge p-i-n APD⁴³⁻⁴⁵, did not meet such a criterion, and the solution relies on engineering an electric field distribution so that the low-quality material regions, especially the regions that are etched, are free from the high electric fields. Here the demonstrated GeSi SPAD achieves its high performance through optimizing the epitaxial recipe with ultrahigh-vacuum CVD, the profile of post-epitaxy thermal annealing, the process of surface passivation, and the dopant implementation to control the electric field distribution.

Fig. 2 shows the cross-sectional scanning-electron-microscope (SEM) image of the fabricated GeSi SPAD. The device fabrication starts with phosphorus (P) implants over a silicon-on-insulator (SOI) wafer to form the deep n-well region and the lower part of the n-sinker region in Si, followed by an epitaxial growth of 250 nm Si (multiplication layer) on the SOI wafer with ultrahigh-vacuum CVD. The buried SiO₂ of the SOI wafer is used to isolate the leakage current from the bulk Si substrate. Boron (B) implants form the charge layer region in Si, and P implants form the upper part of the n-sinker and the n-contact doping regions in Si, followed by another epitaxial growth of buffer Si, thin SiGe, and 450 nm Ge (absorption layer). After a post-epitaxy thermal annealing, a series of dry and wet etches form a GeSi mesa, where polycrystalline-Si based passivation is processed over the GeSi mesa surfaces including the top surface and sidewall. B implants form the p-contact doping region in Ge, followed by silicide process to create the ohmic contacts over both n-contact and p-contact doping regions, and Al metallization process to define the electrical traces and pads for electrical probing. Finally, SiN is deposited and etched to form an anti-reflection coating (ARC) layer on top of the GeSi mesa for optical illumination.

Fig. 3 (a) shows the IV measurement from wafer-level testing where the reverse-bias current is plotted as a function of the applied voltage, with and without a collimated 1310 nm laser beam to illuminate the device under testing (DUT). Two DUT named S1 and S2 are given, and they are of the same 15 μm diameter device except the charge layer concentration of S1 is slightly larger than that of S2. A reference PD, i.e., the same 15 μm diameter device except its charge layer is removed, shows a photocurrent about 1 μA under the same measurement conditions. By using this number and intercepting the photocurrents in Fig. 3 (a), the corresponding primary (i.e., at unity gain point) dark currents of S1 and S2 are determined to be about the same 8 pA at -9.2 V and -8.8V, respectively, corresponding to 4.5 μA/cm² and is the lowest value ever reported for Ge-based APD and/or SPAD. Additional IV measurements show that the primary dark current is increased by about 12 times when the device diameter is increased from 15 μm to 50 μm, suggesting that the primary dark current scales reasonably well with the device area. The punch-through voltage V_{PT} of S1 and S2 are determined to be -9.3 V and -9 V, respectively, from additional CV measurements and coinciding with the “knee” points of the photocurrents in Fig. 3 (a). The breakdown voltage V_{BD} of S1 and S2 are determined to be -10.3 V and -10.9 V, respectively, by defining 10 μA dark current as the breakdown point. Moreover, the breakdown voltage thermal coefficient, defined as $(\Delta V_{BD} / V_{BD}) / \Delta T$ where ΔV_{BD} and ΔT are the increments of breakdown voltage and temperature, is determined from additional temperature-dependent IV measurements to be about 0.06 %/°C between 30°C and 80°C, which agrees reasonably with the case of Si pin APD⁴⁶. The voltage differences between V_{BD} and V_{PT} for S1 and S2 are 1 V and 1.9 V, respectively, which manifest the difference in charge layer concentrations. Interestingly, it can be observed that the shapes of the photo IV curve and the corresponding dark IV curve in Fig. 3 (a) share striking similarities, so we plot the photocurrent gain and the corresponding dark current gain as a function of the applied voltage in Fig. 3 (b) for comparison. It is found that they overlap closely with each other up to gain about a hundred, suggesting that the multiplied component of the dark current originates mostly away from the low-quality material regions around the GeSi mesa periphery.

To characterize the performance of the demonstrated GeSi SPAD, gated-mode operation²²⁻²⁸ is applied in which the cathode of the DUT is biased repeatedly at repetition time T_r through a bias-Tee with a DC voltage below V_{BD} and a radio-frequency (RF) voltage pulse causing a total operation voltage above V_{BD} during gate time T_g . The breakdown current at the anode of the DUT is terminated with a 50Ω load, and the resultant voltage signal is then amplified by a low-noise amplifier and fed to either a counter or an oscilloscope to record the counting events (for more details see the section of Methods). Since T_g is typically around a few or tens of nanoseconds, DCR below GHz or sub-GHz range can be time-resolved and hence gated-mode operation has been used in characterizing SPADs that may have wide ranges of DCRs. In Fig. 4 (a), the measured DCR from die-level testing is plotted as a function of excess bias V_{ex} (i.e., the difference voltage between the operation voltage above V_{BD} and V_{BD}) for S1 and S2 using the counter, given T_g and T_r equal to 5 ns and 102.4 ns, respectively. DCR between 8 kHz/ μm^2 and 90 kHz/ μm^2 can be reached for V_{ex} between 0.5V and 2.5V (i.e., about 2 % and 25 % of V_{BD}), which are the lowest values ever reported for Ge-based SPAD. Next, 1310 nm picosecond laser pulses in synchronization with gate pulses are injected into a confocal microscope setup that couples to the device (for more details see the section of Methods). The average number of photons per pulse $\langle n \rangle$ is controlled by first calibrating the optical loss of coupling the confocal microscope to the device and then adjusting a variable optical attenuator that attenuates the laser pulses. SPDP can be obtained by subtracting the measured DCR from the measured total count rate (TCR), i.e., the count rate with the pulsed laser turned on, and multiplying it by $T_g / \langle n \rangle$ assuming $\langle n \rangle \ll 1$ to ensure the probability for a laser pulse containing multiple photons is negligible. In Fig. 4 (b), the measured SPDP is plotted as a function V_{ex} for S1 and S2 using the counter, given the same conditions of T_g and T_r as in Fig. 4 (a). SPDP between 5 % and 30 % can be reached for V_{ex} between 0.5V and 2.5V given $\langle n \rangle = 0.1$. Note that by picking a constant DCR in Fig. 4 (a), e.g., 20 kHz/ μm^2 , and finding the corresponding SPDP in Fig. 4 (b), e.g., 12 % and 7 % for S1 and S2, respectively, S1 is determined to perform better than S2. Such a result can be explained by, when the high electric field penetrating into the Ge region for S1 is similar to that for S2, the voltage drop in the Si region for S1 is higher than that for S2 due to the higher charge layer concentration, which leads to similar DCR but higher SPDP for S1. In Fig. 4 (c), the measured timing jitter δ in full-width-half-maximum (FWHM) is plotted as a function V_{ex} for S1 and S2 using the oscilloscope, given the same conditions of T_g and T_r as in Fig. 4 (b). δ between 110 ps and 210 ps can be reached for V_{ex} between 0.5V and 2.5V given $\langle n \rangle = 10$. Finally, exemplary voltage waveforms from the DCR measurement of S1 in Fig. 4 (a) operated at V_{ex} equal to 1 V, 1.5 V, and 2 V are shown in Fig. 4 (d), where sharp signal rise due to breakdown and sharp signal fall due to gate-on turned gate-off are observed. Also, exemplary photon arrival histogram from the δ measurement of S1 in Fig. 4 (c) operated at V_{ex} equal to 2 V is shown in Fig. 4 (e), where δ of 110 ps is observed and attributed mainly to the device δ since the system δ is estimated to be around a few tens of picoseconds and is negligible.

When a breakdown event occurs and induces strong current flow passing through the multiplication region, some carriers may be trapped in defects and subsequently released at a time delay causing another breakdown event. Such a phenomenon is called after-pulsing, and its occurrence probability APP and characteristic time τ are crucial parameters in SPAD operations. For free-running-mode operation^{17,18}, if the after-pulsing event occurs during the recovery phase of quenching, long digital pulse can appear and spoil the following counting events¹⁷. Consequently, the hold-off time of a quenching circuit is typically set to a similar or larger time scale compared to τ (depending on the acceptable APP) to avoid long digital pulse, which limits the maximum count rate in free-running-mode operation. For gated-mode operation²²⁻²⁸, after-pulsing event effectively increases the DCR so T_r is usually set to a similar or larger time scale compared to τ (depending on the acceptable APP) to avoid excessive DCR, and hence limits the maximum count rate in gated-mode operation. In the literature, attempts to characterize the after-pulsing of Ge-based SPAD have been made, but either the results are over-shadowed by the high DCR^{24,25} or the reported APP and τ are limited to being operated at a low temperature²⁷, which significantly increases the effect of after-pulsing. Here we characterize the after-pulsing of the demonstrated GeSi SPAD at room temperature, by applying time-correlated counting under gated-mode operation to measure the statistics of interarrival time with dark counts^{47,48} (for more details see the section of Methods). In Fig. 5 (a), the measured histograms for interarrival time normalized by T_r are shown for several V_{ex} , given the same conditions of T_g and T_r as in Fig. 4. The black dashed lines are fitting curves for the thermally-generated counts $n_{TG}(i)$, whereas the after-pulsing counts $n_{AP}(i)$ are above the fitting curves and distribute exponentially. i is the index representing the i th gate time after the reference gate time. By fitting $n_{AP}(i)$ with an exponential probability density function $\gamma e^{-i/\tau}$, τ can be calculated by

$$\tau = \frac{T_r}{\ln\left(\frac{n_{AP}(1)}{n_{AP}(2)}\right)}, \quad (2)$$

and APPs can be calculated by

$$APP(i) = \frac{n_{AP}(i)}{1 + \sum_{i=1}^{\infty} n_{TG}(i)} \quad \text{and} \quad APP' = \frac{n_{AP}}{\left(1 + \sum_{i=1}^{\infty} n_{TG}(i)\right) \cdot \frac{T_r}{T_g}}, \quad (3)$$

where $n_{AP}(i) = \int_{iT_r}^{iT_r+T_g} \gamma e^{-t/\tau} dt$ and $n_{AP} = \int_0^{\infty} \gamma e^{-t/\tau} dt$. Here, the interpretation of $APP(i)$ is, under gated-mode operation, the probability of finding an after-pulsing event during the i th gate time when a dark count occurs during the reference gate time. And, the interpretation of APP' is, under free-running-mode operation, the total probability of finding an after-pulsing event when a dark count occurs. In Fig. 5 (b), the calculated τ is shown as a function of V_{ex} . It is observed that τ is relatively insensitive to V_{ex} and is about 90 ns for V_{ex} between 1 V and 2 V. In Fig. 5 (c), the calculated $APP(1)$, $APP(2)$, and APP' are shown as a function of V_{ex} . It is observed that APP' is

exponentially related to V_{ex} and is between 0.7 % and 2 % for V_{ex} between 1 V and 2 V. The numbers of τ and APP' are found to be in reasonable agreement with those of the Si-based SPADs at room temperature⁴⁹, suggesting the high crystalline quality of the demonstrated GeSi SPAD.

As proof of concept, the measurement setup for producing data shown in Fig. 4 and 5 is modified to apply the demonstrated GeSi SPAD for LiDAR based on direct TOF technique. 3D scanning and imaging are done by replacing the variable optical attenuator with a coaxial transceiver that uses x-y galvo-mirrors to steer the fired laser pulses and collect the returned laser pulses along the same optical path. The mirrors are angular-direction-controlled between x-y angles equal to $(-6^\circ, 4^\circ)$ to $(9^\circ, -5^\circ)$ in a feedback loop such that the laser pulses are projected according to the angular directions following the steering commands (for more details see the section of Methods). At every steering command, the acquired histogram from the counter is analyzed and the temporal location of its peak is identified and translated into the corresponding x, y, z positions in the PCL dataset. For this experiment T_g and T_r are set to be equal to 5 ns and 250 ns, respectively, and since T_g is only 5 ns the maximum TOF range is limited to 75 cm. Consequently, a space that spans roughly 0.5 m^3 is prepared and filled with a series of 3D objects for photo shoot. As shown by the 2D RGB image in Fig. 6 (a), the 3D objects are placed against the wall at different distances away from the mirrors under regular indoor ceiling lighting. Alphabet letters standing on the lower cardboard staircase are of 100 mm in height, and the platonic solids standing on the upper cardboard staircase are of 65 mm in height. In Fig. 6 (b), the captured 3D PCL image is shown, in which the relative distances away from the mirrors are color-coded for better visualization. It can be clearly seen that the spatial orientations of the 3D objects are nicely revolved without any post-processing, attesting to the potential of the demonstrated GeSi SPAD for LiDAR based on direct TOF technique.

To summarize, we demonstrate the Geiger-mode operation of a high-performing GeSi APD as SPAD at room temperature. With a low breakdown voltage of 10.3 V and a small excess bias of 0.75 V, DCR, SPDP, and timing jitter are respectively measured to be $19 \text{ kHz}/\mu\text{m}^2$, 12 %, and 188 ps at 1310 nm wavelength. The corresponding NEP is calculated to be $3 \text{ fW}/\sqrt{\text{Hz}}$ at room temperature, which is 2 to 3.5 orders of magnitude lower than that of the previously reported Ge-base SPADs if they were operated at 300 K. By measuring the statistics of interarrival time with dark counts, total probability and characteristic time of after-pulsing are respectively determined to be $< 1 \%$ and about 90 ps, matching well with the numbers of Si-based SPADs at room temperature. 3D scanning and imaging of 3D objects are successfully demonstrated by applying the high-performing GeSi SPAD for direct TOF technique based LiDAR. Our work brings forth the room temperature operation of high-performing GeSi SPAD from low temperature, which was previously deemed not possible, and shall be a strong contender in the quest of room temperature operated, CMOS compatible, SWIR single-photon detectors. In addition, since Ge-based detector operated in linear-mode has been commercialized through silicon photonic platform³⁷ and CMOS image sensor platform⁵⁰, the capability of operating in Geiger-mode shall boost the developments of optoelectronic devices and circuits over these platforms toward unprecedented single-photon level sensitivity.

Methods

The electrical and optical setups shown in Fig. 7 are used for the counting in Fig. 4, the time-correlated counting in Fig. 5, and the 3D scanning and imaging in Fig. 6. All experiments are done in a standard laser lab environment at room temperature. A power supply provides a DC voltage to the DC input port of a bias-Tee (Anritsu K251). A pulse function generator (Keysight 81150A) provides a RF voltage pulse to the RF input port of the bias-Tee, and triggers the pulsed laser (Picoquant LDH with Taiko PDL driver) with a programmable time delay. The output of the bias-Tee is connected to a custom-made RF probe in which alternating-current (AC) bypass and 50 Ω termination are implemented. A low-noise amplifier (Mini-Circuits ZFL-1000LN+) is used to amplify the voltage signal to be fed to the counter (Picoquant Multiharp 150) or the oscilloscope (Keysight EXR254A). The output of the pulsed laser is 1 % split for optical power monitoring and 99 % attenuated by a variable optical attenuator (Thorlabs V1000PA). The output of the variable optical attenuator is 10 % split for optical power monitoring and 90% collimated by a collimator. The collimated laser pulses are injected into a custom-made confocal microscope, containing a pellicle beam splitter and an objective lens to respectively reflect and focus the laser pulses toward the device, and another pellicle beam splitter and a tube lens to visually monitor the device with two cameras, one visible and another SWIR. When performing the counting using the counter, either the gate pulse edge or the event pulse edge can be used to trigger the counter, and the counter integration time is set to 100 s. When performing the counting using the oscilloscope, the rising edge of the event pulse is used to trigger the oscilloscope data capturing frame. The timing jitter analysis is performed with the oscilloscope by generating a histogram using the rising edge of the event pulse in reference to the gate pulse over 60 K events. The dark counts and total counts directly reported by the counter or the oscilloscope should be multiplied by T_r / T_g to obtain the measured DCR and TCR. When performing the time-correlated counting, the output of the low-noise amplifier is divided into two channels with equal power by a RF power divider (custom-made), and a small time delay due to a longer RF cable is introduced to one of the two channels. The outputs of the more delayed channel and the other less delayed channel are respectively coupled to the sync and data input ports of the counter to enable the time-correlated counting of interarrival time, and the counter integration time is set to 100 s. When performing the 3D scanning and imaging, the variable optical attenuator is replaced by a coaxial transceiver consisting of a circulator, a collimator, and x-y galvo-mirrors (Thorlabs QS30XY-AG). Note that a 1310 nm CW laser and a 635 nm CW laser are coupled to the same optical path of the pulsed laser, and respectively used to align the focused laser pulses with the device under the confocal microscope and mark the initial angular direction of the mirrors before steering.

References

- [1] Politi, A., Matthews, J. C. F. & O'Brien, J. L. Shor's quantum factoring algorithm on a photonic chip. *Science* **325**, 1221 (2009).
- [2] Zhong, H.-S. *et al.* Quantum computational advantage using photons. *Science* **370**, 1460–1463 (2020).

- [3] Waks, E. *et al.* Quantum cryptography with a photon turnstile. *Nature* **420**, 762 (2002).
- [4] Lai, S.-K. *et al.* Satellite-relayed intercontinental quantum network. *Phys. Rev. Lett.* **120**, 030501 (2018).
- [5] Brida, G., Genovese, M. & Ruo Berchera, I. Experimental realization of sub-shot-noise quantum imaging. *Nat. Photon.* **4**, 227–230 (2010).
- [6] Zarghami, M. *et al.* A 32×32-pixel CMOS imager for quantum optics with per-SPAD TDC, 19.48% fill-factor in a 44.64- μm pitch reaching 1-MHz observation rate. *IEEE J. Solid-State Circuits* **55**, 2819–2830 (2020).
- [7] Bruschini, C., Homulle, H., Antolovic, I. M., Burri, S. & Charbon E. Single-photon avalanche diode imagers in biophotonics: review and outlook. *Light Sci. Appl.* **8**, 87 (2019).
- [8] Pawlikowska, A. M., Halimi, A., Lamb, R. A. & Buller, G. S. Single-photon three-dimensional imaging at up to 10 kilometers range. *Opt. Express* **25**, 11919–11931 (2017).
- [9] Kuzmenko, K. *et al.* 3D LIDAR imaging using Ge-on-Si single-photon avalanche diode detectors. *Opt. Express* **28**, 1330–1344 (2020).
- [10] Entwistle, M. *et al.* Geiger-mode APD camera system for single photon 3-D LADAR imaging. *Proc. SPIE* **8375**, 83750D (2012).
- [11] Morimoto, K. *et al.* Megapixel time-gated SPAD image sensor for 2D and 3D imaging applications. *Optica* **7**, 346–354 (2020).
- [12] Hadfield, R. H. Single-photon detectors for optical quantum information applications. *Nat. Photon.* **3**, 696–705 (2009).
- [13] Marsili, F. *et al.* Detecting single infrared photons with 93% system efficiency. *Nat. Photon.* **7**, 210–214 (2013).
- [14] Najafi, F. *et al.* On-chip detection of non-classical light by scalable integration of single-photon detectors. *Nat. Commun.* **6**, 5873 (2015).
- [15] Lacaíta, A., Zappa, F., Cova, S. & Lovati, P. Single-photon detection beyond 1 μm : performance of commercially available InGaAs/InP detectors. *Appl. Opt.* **35**, 2986–2996 (1996).
- [16] Fang, Y.-Q. *et al.* InGaAs/InP single-photon detectors with 60% detection efficiency at 1550 nm. *Rev. Sci. Instrum.* **91**, 083102 (2020).
- [17] Xu, H., Pancheri, L., Dalla Betta, G.-F. & Stoppa, D. Design and characterization of a p+/n-well SPAD array in 150nm CMOS process. *Opt. Express* **25**, 12765–12778 (2017).
- [18] Lee, M.-J. *et al.* High-performance back-illuminated three-dimensional stacked single-photon avalanche diode implemented in 45-nm CMOS technology. *IEEE J. Sel. Top. Quantum Electron.* **24**, 3801809 (2018).
- [19] Sliney, D. H. & Freasier, B. C. Evaluation of optical radiation hazards. *Appl. Opt.* **12**, 1–24 (1973).
- [20] Bird, R. E., Hulstrom, R. L. & Lewis, L. J. Terrestrial solar spectral data sets. *Sol. Energy* **30**, 563–574 (1983).
- [21] Arnulf, A., Bricardi, J., Cura, E. & Varet, C. Transmission by haze and fog in the spectral region 0.35 to 10 microns. *J. Opt. Soc. Am.* **47**, 491–498 (1957).
- [22] Loudon, A. Y. *et al.* Enhancement of the infrared detection efficiency of silicon photon-counting avalanche photodiodes by use of silicon germanium absorbing layers. *Opt. Lett.* **27**, 219–221 (2002).
- [23] Tosi, A., Dalla Mora, A., Zappa, F. & Cova, S. Germanium and InGaAs/InP SPADs for single-photon detection in the near-infrared. *Proc. SPIE* **6771**, 67710P (2007).
- [24] Lu, Z. *et al.* Geiger-mode operation of Ge-on-Si avalanche photodiodes. *IEEE J. Quantum Electron.* **47**, 731–735 (2011).
- [25] Warburton, R. E. *et al.* Ge-on-Si single-photon avalanche diode detectors: design, modeling, fabrication, and characterization at wavelengths 1310 and 1550 nm. *IEEE Trans. Electron. Devices* **60**, 3807–3813 (2013).
- [26] Martinez, N. J. D. *et al.* Single photon detection in a waveguide-coupled Ge-on-Si lateral avalanche photodiode. *Opt. Express* **25**, 161310–16139 (2017).
- [27] Vines, P. *et al.* High performance planar germanium-on-silicon single-photon avalanche diode detectors. *Nat. Commun.* **10**, 1086 (2019).
- [28] Ferre Llin, L. *et al.* High sensitivity Ge-on-Si single-photon avalanche diode detectors. *Opt. Lett.* **45**, 6406–6409 (2020).
- [29] Ke, S. *et al.* Design of wafer-bonded structures for near room temperature Geiger-mode operation of germanium on silicon single-photon avalanche photodiode. *Appl. Opt.* **56**, 4646–4653 (2017).
- [30] Soref, R. A., De Leonardis, F. & Passaro, V. M. N. Simulations of nanoscale room temperature waveguide-coupled single-photon avalanche detectors for silicon photonic sensing and quantum applications. *ACS Appl. Nano Mater.* **2**, 7503–7512 (2019).
- [31] Thorburn, F. *et al.* Ge-on-Si single-photon avalanche diode detectors for short-wave infrared wavelengths. *J. Phys. Photonics* **4**, 012001 (2022).

- [32] Samavedam, S. B., Currie, M. T., Langdo, T. A. & Fitzgerald, E. A. High-quality germanium photodiodes integrated on silicon substrates using optimized relaxed graded buffers. *Appl. Phys. Lett.* **73**, 2125–2127 (1998).
- [33] Luan, H.-C. *et al.* High-quality Ge epilayers on Si with low threading-dislocation densities. *Appl. Phys. Lett.* **75**, 2909–2911 (1999).
- [34] Osmond, J. *et al.* Ultralow dark current Ge/Si(100) photodiodes with low thermal budget. *Appl. Phys. Lett.* **94**, 201106 (2009).
- [35] Åberg, I. *et al.* A low dark current and high quantum efficiency monolithic germanium-on-silicon CMOS imager technology for day and night imaging applications. *International Electron Devices Meeting (IEDM)*, pp. 14.4.1-14.4.4 (2010).
- [36] Lee, K.-H. *et al.* Defects reduction of Ge epitaxial film in a germanium-on-insulator wafer by annealing in oxygen ambient. *APL Mater.* **3**, 016102 (2015).
- [37] Morse, M., Dosunmu, O., Sarid, G. & Chetrit, Y. Performance of Ge-on-Si p-i-n photodetectors for standard receiver modules. *IEEE Photon. Technol. Lett.* **18**, 2442-2444 (2006).
- [38] Takenaka, M., Morii, K., Sugiyama, M., Nakano, Y. & Takagi, S. Dark current reduction of Ge photodetector by GeO₂ surface passivation and gas-phase doping. *Opt. Express* **20**, 8718–8725 (2012).
- [39] Sammak, A., Aminian, M., Nanver, L. K. & Charbon, E. CMOS-Compatible PureGaB Ge-on-Si APD Pixel Arrays. *IEEE Trans. Electron. Devices* **63**, 92–99 (2016).
- [40] Kang, Y. *et al.* Monolithic germanium/silicon avalanche photodiodes with 340 GHz gain–bandwidth product. *Nat. Photon.* **3**, 59–63 (2008).
- [41] Duan, N., Liow, T.-Y., Lim, A. E.-J., Ding, L. & Lo, G. Q. 310 GHz gain-bandwidth product Ge/Si avalanche photodetector for 1550 nm light detection. *Opt. Express* **20**, 11031–11036 (2012).
- [42] Huang, M. *et al.* Germanium on silicon avalanche photodiode. *IEEE J. Sel. Top. Quantum Electron.* **24**, 3800911 (2018).
- [43] Assefa, S., Xia, F. & Vlasov, Y. A. Reinventing germanium avalanche photodetector for nanophotonic on-chip optical interconnects. *Nature* **464**, 80–84 (2010).
- [44] Virost, L. *et al.* Germanium avalanche receiver for low power interconnects. *Nat. Commun.* **5**, 4957 (2014).
- [45] Chen, H. T. *et al.* High sensitivity 10Gb/s Si photonic receiver based on a low-voltage waveguide-coupled Ge avalanche photodetector. *Opt. Express* **23**, 815–822 (2015).
- [46] Su, Y. K., Chang, C. Y. & Wu, T. S. Temperature dependent characteristics of a PIN avalanche photodiode (APD) in Ge, Si and GeAs. *Opt. Quant. Electron.* **11**, 109–117 (1979).
- [47] Hofbauer, M., Steindl, B. & Zimmermann, H. Temperature dependence of dark count rate and after pulsing of a single-photon avalanche diode with an integrated active quenching circuit in 0.35 μ m CMOS. *J. Sens.* **2018**, 9585931 (2018).
- [48] Mahmoudi, H., Hofbauer, M., Goll, B. & Zimmermann, H. Noise and breakdown characterization of SPAD detectors with time-gated photon-counting operation. *Sensors* **21**, 5287 (2021).
- [49] Ziarkash, A. W., Joshi, S. K., Stipčević, M. & Ursin, R. Comparative study of afterpulsing behavior and models in single photon counting avalanche photo diode detectors. *Sci. Rep.* **8**, 5076 (2018).
- [50] Na, N. *et al.* High-performance germanium-on-silicon lock-in pixels for indirect time-of-flight applications. *International Electron Devices Meeting (IEDM)*, pp. 32.4.1-32.4.4 (2018).

Author contributions

N. N. conceived the design and supervised the project. Y.-C. Lu contributed to device simulation, layout synthesis, and wafer-level data analysis. Y.-H. L. contributed to layout synthesis, process integration, and wafer-level data analysis. P.-W. C. and Y.-C. Lai contributed to process integration and device fabrication. Y.-R. L. contributed to process integration and wafer-level data analysis. C.-C. L. contributed to wafer-level data collection. T. S. contributed to die-level data collection and 3D PCL image capture. C.-H. C. contributed to die-level data analysis. S.-L. C. oversaw the project.

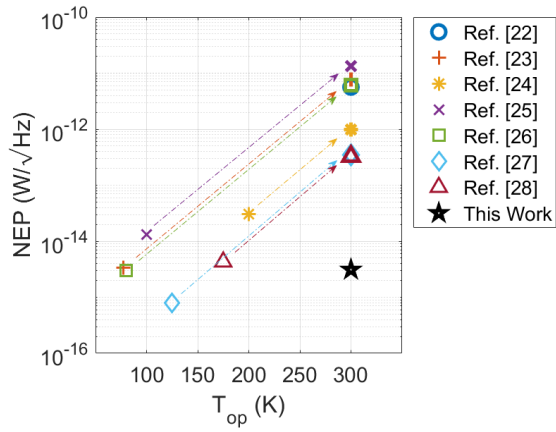


Fig. 1 | NEP and operation temperature of the reported Ge-based SPADs. The dashed-dotted arrows indicate the NEP of the previously-reported Ge-based SPADs if they were operated at 300 K, assuming DCR is doubled for every 10 K increase in temperature. Note that all devices are tested at 1310 nm wavelength except for Ref. [22] at 1210 nm.

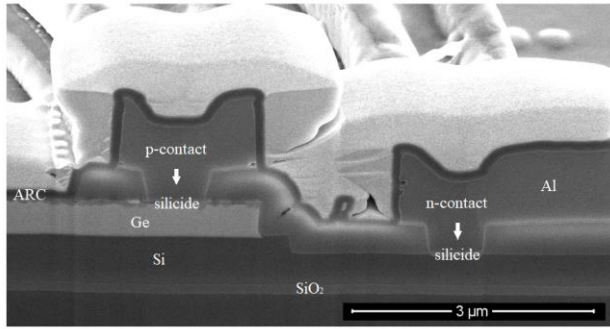


Fig. 2 | SEM cross-sectional view of the demonstrated GeSi SPAD. Note the image is captured near the GeSi mesa sidewall to have an overview of the main elements of the device. Pt, i.e., the white conformal layer, is deposited over the device to avoid SEM charging. B implants are used to create the p-contact region in Ge, and P implants are used to create the n-contact region in Si. Additional B implants in Si form the charge layer region below Ge, and additional P implants in Si form the deep n-well region above the buried SiO₂, and the n-sinker region between the n-contact region and the deep n-well region.

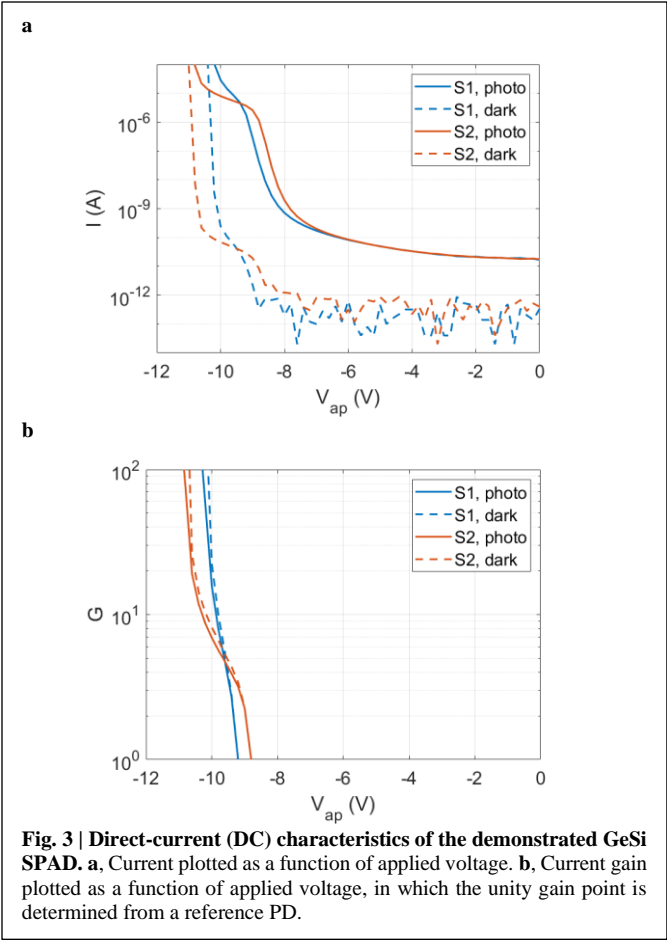
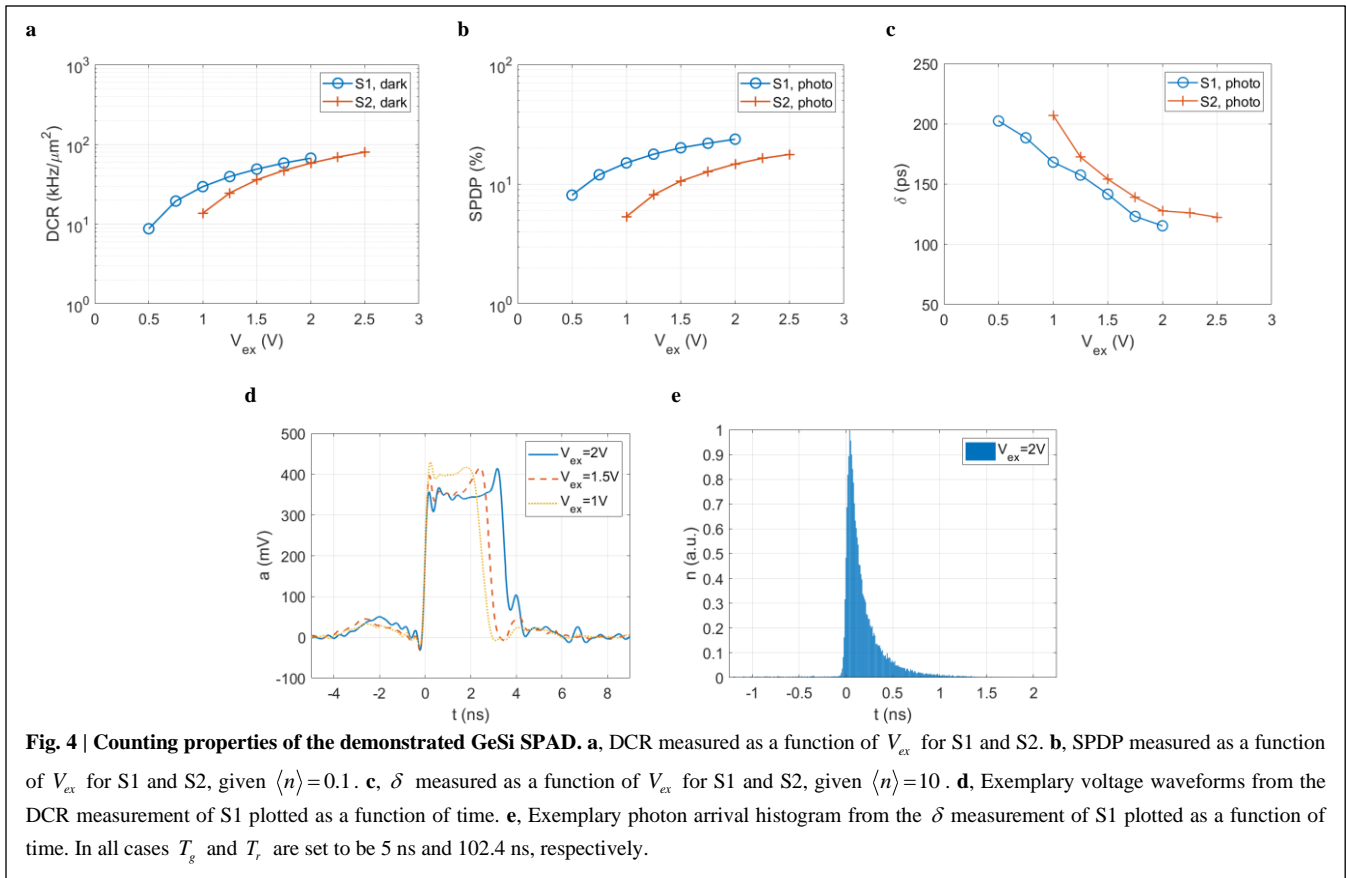


Fig. 3 | Direct-current (DC) characteristics of the demonstrated GeSi SPAD. a, Current plotted as a function of applied voltage. **b,** Current gain plotted as a function of applied voltage, in which the unity gain point is determined from a reference PD.



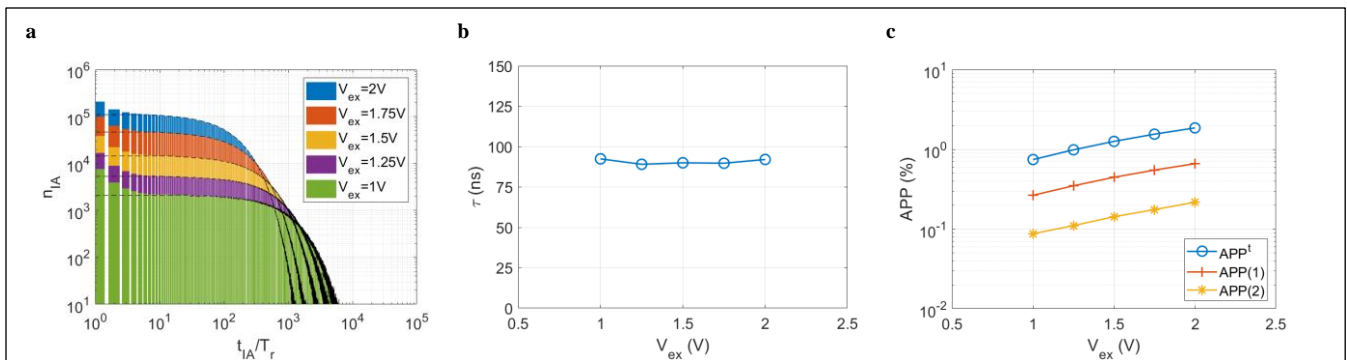
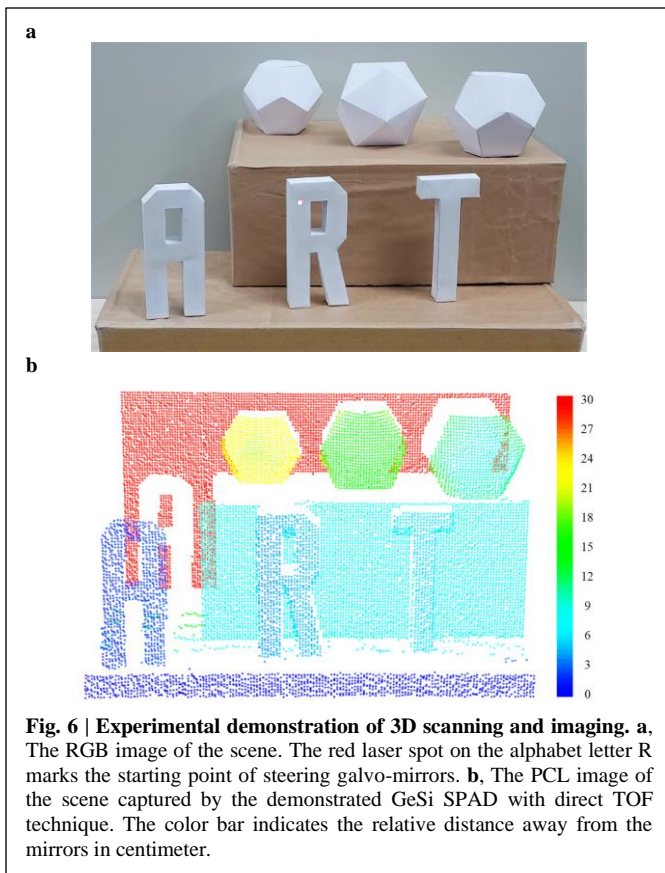


Fig. 5 | After-pulsing investigated by time-correlated counting. **a**, Interarrival time histogram plotted as a function of interarrival time normalized by T_r . **b**, τ calculated by Eq. (2) with the data in Fig. 5 (a), and plotted as a function of V_{ex} . **c**, APP calculated from Eq. (3) with the data in Fig. 5 (a) and (b), and plotted as a function of V_{ex} . In all cases T_g and T_r are set to be 5 ns and 102.4 ns, respectively.



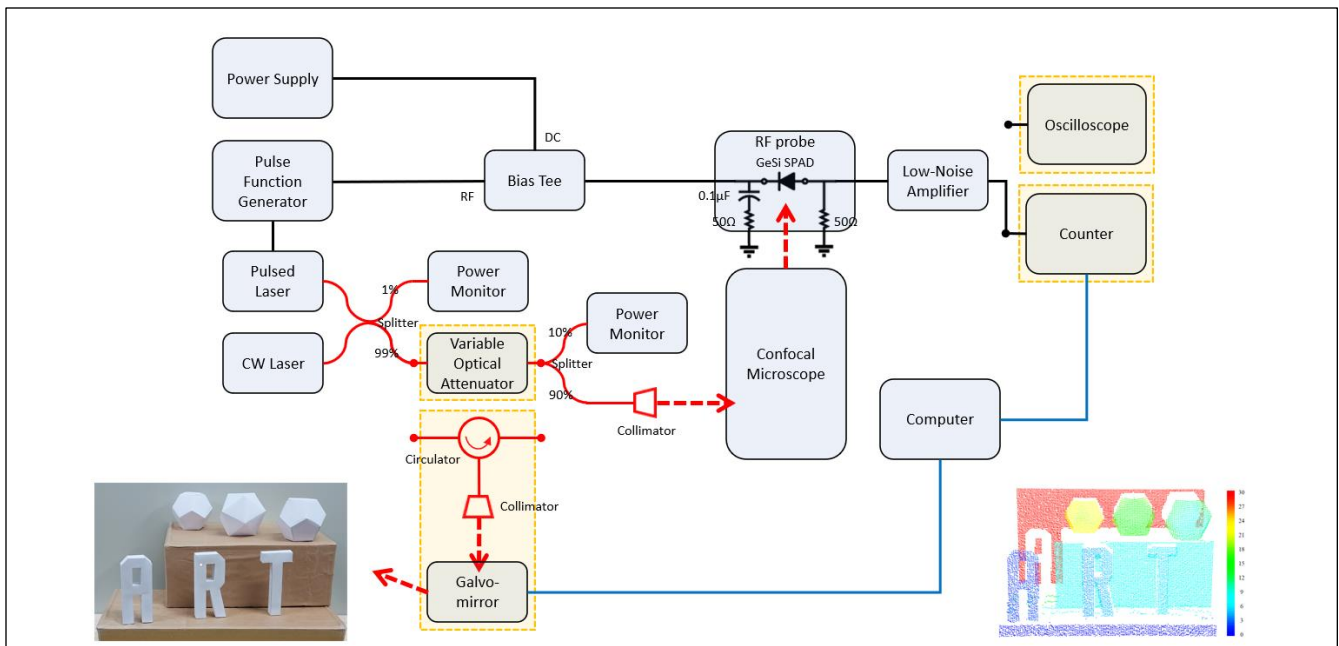


Fig. 7 | The schematic plot of the electrical and optical setups used in producing data shown in Fig. 4, 5, and 6.